Article

Untying the insulating and superconducting orders in magic-angle graphene

Petr Stepanov[1], Ipsita Das[1], Xiaobo Lu[1], Ali Fahimniya[2], Kenji Watanabe[3], Takashi Taniguchi[3], Frank H. L. Koppens[1], Johannes Lischner[4], Leonid Levitov[2] & Dmitri K. Efetov[1✉]

The coexistence of superconducting and correlated insulating states in magic-angle twisted bilayer graphene[1–11] prompts fascinating questions about their relationship. Independent control of the microscopic mechanisms that govern these phases could help uncover their individual roles and shed light on their intricate interplay. Here we report on direct tuning of electronic interactions in this system by changing the separation distance between the graphene and a metallic screening layer[12,13]. We observe quenching of correlated insulators in devices with screening layer separations that are smaller than the typical Wannier orbital size of 15 nanometres and with twist angles that deviate slightly from the magic angle of 1.10 ± 0.05 degrees. Upon extinction of the insulating orders, the vacated phase space is taken over by superconducting domes that feature critical temperatures comparable to those in devices with strong insulators. In addition, we find that insulators at half-filling can reappear in small out-of-plane magnetic fields of 0.4 tesla, giving rise to quantized Hall states with a Chern number of 2. Our study suggests re-examination of the often-assumed 'parent-and-child' relation between the insulating and superconducting phases in moiré graphene, and suggests a way of directly probing the microscopic mechanisms of superconductivity in strongly correlated systems.

Strongly correlated electron systems exhibit a variety of interactions and emergent orders. Famously, the coexistence of unconventional superconductivity and correlated insulating phases in cuprates, pnictides and heavy fermion compounds[14], has led to the conjecture that superconductivity could be assisted by correlated insulating order, thus arising from a purely electronic mechanism. Achieving direct control of electron–electron interactions—a long-standing goal in the study of correlated electron systems—would clarify the separate origin and the complex relation between these phases. However, previous attempts to control electron–electron interactions in other crystalline correlated systems were impeded by small atomic orbital sizes and strong sensitivity to doping[15].

Magic-angle twisted bilayer graphene (MATBG), consisting of two vertically stacked graphene sheets that are slightly misaligned by the magic angle $\theta = \theta_m \approx 1.1°$, has emerged recently as a new correlated system. Flat moiré bands in MATBG[1–11] and similar "twistronic" systems[16,17] host strongly correlated electrons that exhibit a variety of interesting ordered states, notably correlated insulators[1,4,5], superconductors[2–5], magnets and topological states[5–7]. Initial experiments unveiled correlated insulators at integer occupancies of the moiré bands coexisting with superconducting domes appearing upon slight additional doping[2,18–22]. The coexistence of these orders was taken as an indication that they are directly related and arise from a common mechanism, similar to the scenarios that have been proposed for the cuprates[14].

The exceptionally large moiré unit cell in MATBG enables novel methods for testing this hypothesis. In the Mott–Hubbard picture, the condition for the appearance of correlated insulators is a large ratio of the on-site Coulomb energy U and the kinetic energy t, $U/t \gg 1$. In MATBG t can be increased by tuning θ away from θ_m, which 'unflattens' the flat bands. The energy U can be controlled independently by changing the dielectric environment. If the distance w between MATBG and a metallic layer is made smaller than the moiré unit cell size, $w < \lambda \approx 15$ nm, polarization charges will screen out the Coulomb interactions on that scale and suppress U (refs. [12,13]) (Fig. 1a, b and Supplementary Information).

Here we report on transport measurements in screening-controlled MATBG devices with several near-magic-angle twist angles. We find a strong suppression of the correlated insulators when metallic graphite screening layers are placed closer than 10 nm from the MATBG plane, separated from it by insulating multilayers of hexagonal boron nitride (hBN), and θ tuned slightly away from 1.1° by ±0.05°. Rather than being weakened, superconductivity persists in the absence of the correlated insulators, taking over the phase space vacated by the correlated insulators and spanning wide doping regions without interruption. This is in contrast to all previous studies, where metallic layers were placed >30 nm away from the MATBG[1–5], and superconductivity regions were found only in the presence of correlated insulators. These observations suggest that the insulating and superconducting orders—rather than sharing a common origin—compete with each other, which calls into question a simple analogy with the cuprates.

[1]ICFO—Institut de Ciencies Fotoniques, The Barcelona Institute of Science and Technology, Barcelona, Spain. [2]Department of Physics, Massachusetts Institute of Technology, Cambridge, MA, USA. [3]National Institute for Materials Science, Tsukuba, Japan. [4]Departments of Materials and Physics and the Thomas Young Centre for Theory and Simulation of Materials, Imperial College London, London, UK. ✉e-mail: dmitri.efetov@icfo.eu
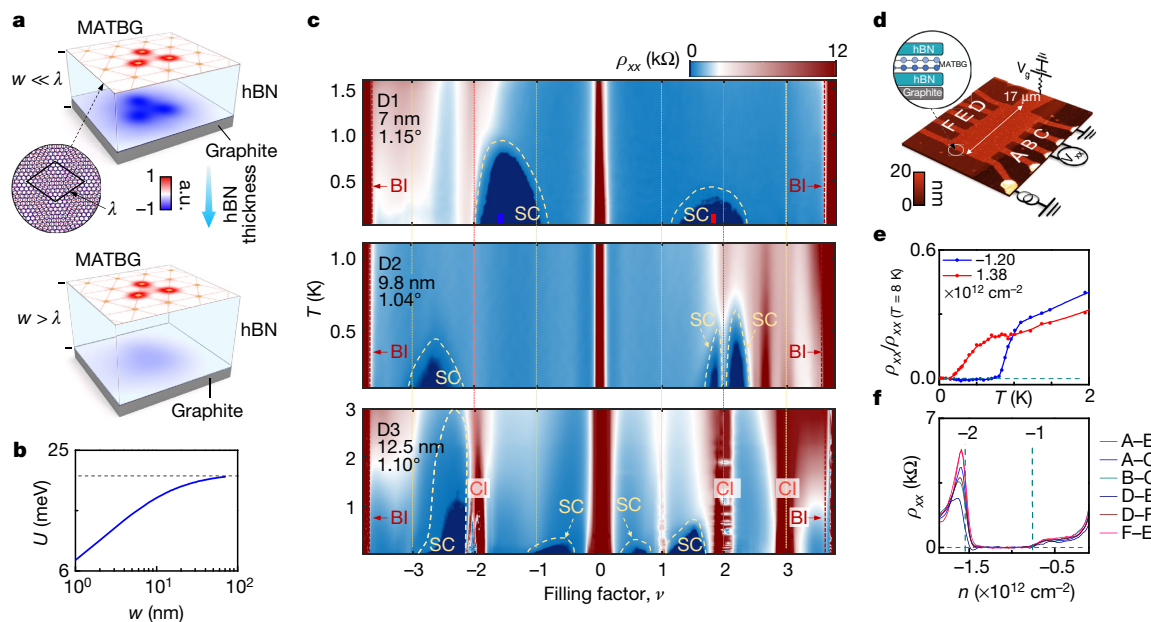
Fig. 1 | Screening-controlled MATBG phase diagrams for near-magic twist angles. a, Wannier orbitals (red) in MATBG are screened by image charges on the graphite surface (blue), where λ is the moiré lattice constant and w is the hBN spacer thickness. **b**, Calculated on-site Coulomb energy U versus w for $\theta = 1.05°$ (dashed line marks the unscreened value). **c**, Colour plot of resistivity ρ_{xx} versus moiré band filling factor ν and temperature T for three screening-controlled MATBG devices (D1) $w \approx 7$ nm, $\theta \approx 1.15°$; (D2) $w \approx 9.8$ nm, $\theta \approx 1.04°$ and (D3) $w \approx 12.5$ nm, $\theta \approx 1.10°$. Signatures of correlated insulators (CI) are completely absent in devices with the thinnest w (D1 and D2), while

superconductivity (SC) persists and T_c values remain virtually unaffected. BI, band insulator. **d**, AFM image and measurement scheme for device D1, a graphite/hBN/MATBG/hBN stack in which the graphite flake acts as the screening layer as well as the back gate. **e**, Normalized ρ_{xx} versus T shows superconductivity transitions for both superconductivity domes in D1, taken at the carrier densities n marked in **c**. **f**, Four-probe resistivity ρ_{xx} versus n for different contact pairs of D1 shows homogeneous distribution of superconductivity across the entire device, measured by different contact pairs, A to F.

Our main findings are illustrated in the phase diagrams of three representative devices with parameters $w \approx 7$ nm, $\theta \approx 1.15°$ (D1); $w \approx 9.8$ nm, $\theta \approx 1.04°$ (D2) and $w \approx 12.5$ nm, $\theta \approx 1.10°$ (D3); the data are presented in Fig. 1c as colour maps and in Fig. 2a as the corresponding line cuts. Figure 1d shows an atomic force microscope image of a typical device (D1), a quadruple van der Waals stack of graphite/hBN/MATBG/hBN, where the bottom hBN layer acts as an ultrathin $w < 15$ nm spacer between the metallic graphite and the MATBG. We use four-terminal resistivity ρ_{xx} measurements; the gate voltage V_g on the graphite layer allows us to capacitively tune the carrier density n which is normalized to n_s, the density of the fully filled fourfold spin/valley degenerate band, which defines the band filling factor $\nu = 4n/n_s$. The positions of $\nu = 0$ mark the charge neutrality point (CNP) of the flat bands, which in all devices shows a small energy gap. It remains, however, unclear whether interaction or trivial band effects break the symmetry at the CNP (Extended Data Fig. 6). Superconductivity in all devices was confirmed by a multitude of tests, including measurements of zero resistance and Fraunhofer interference patterns (Fig. 1e and Extended Data Fig. 4). The high spatial uniformity of our devices (Fig. 1f and Extended Data Fig. 3), allows us to rule out that disorder-induced 'cloaking' could be responsible for the disappearance of the correlated insulators.

Notably, device D1, which has the thinnest w and a θ that is only slightly higher than the magic angle, demonstrates a phase diagram that is very different from those of all previously reported MATBG devices[2–5]. Strikingly, it entirely lacks correlated insulating states, showing clearly metallic $\rho_{xx}(T)$ behaviours at $\nu = \pm 2$, and with ρ_{xx} never exceeding a few kiloOhms (Fig. 2a, b). These observations are in line with the absence of Fermi surface reconstruction at $\nu = \pm 2$, which is evident from the lack of a new sequence of quantum oscillations originating from this point, as well as the very weak Hall density offset in perpendicular magnetic field (Extended Data Figs. 5, 7). Nonetheless, we observe two broad superconductivity domes in both the valence and conduction moiré

bands, with values of $T_c \approx 920$ mK and $T_c \approx 420$ mK, respectively (Fig. 1e). Although these superconductivity states resemble those reported previously, they are not accompanied by correlated insulators and span the integer filling positions.

This behaviour is in contrast to D3, which has the thickest w and a θ that corresponds exactly to θ_m. It shows resistance peaks at all integer
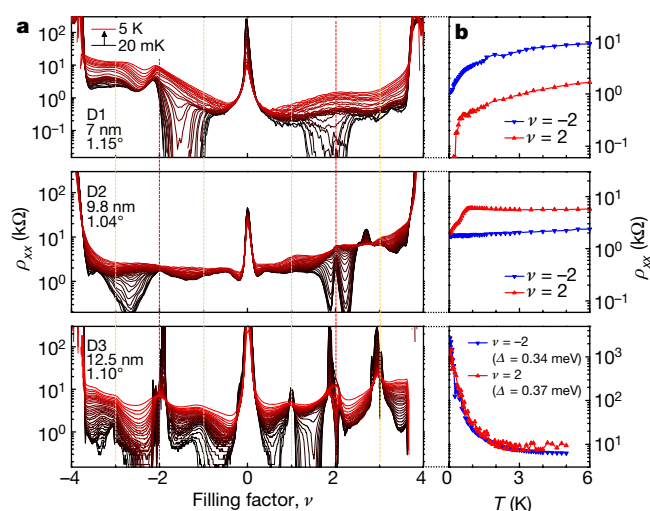

Fig. 2 | The dependence of the superconductivity and correlated insulating phases on temperature and density. a, Line cuts of resistivity ρ_{xx} versus filling factor ν, of devices D1–D3, for different temperatures T from 20 mK to 5 K. **b**, ρ_{xx} versus T for moiré band fillings of $\nu = \pm 2$ for each device. Although D1 and D2 show metallic behaviour in both valence and conduction bands, D3 shows strongly thermally activated behaviour $\rho_{xx} \approx \exp(\Delta/2k_BT)$, consistent with strong correlated insulating order.
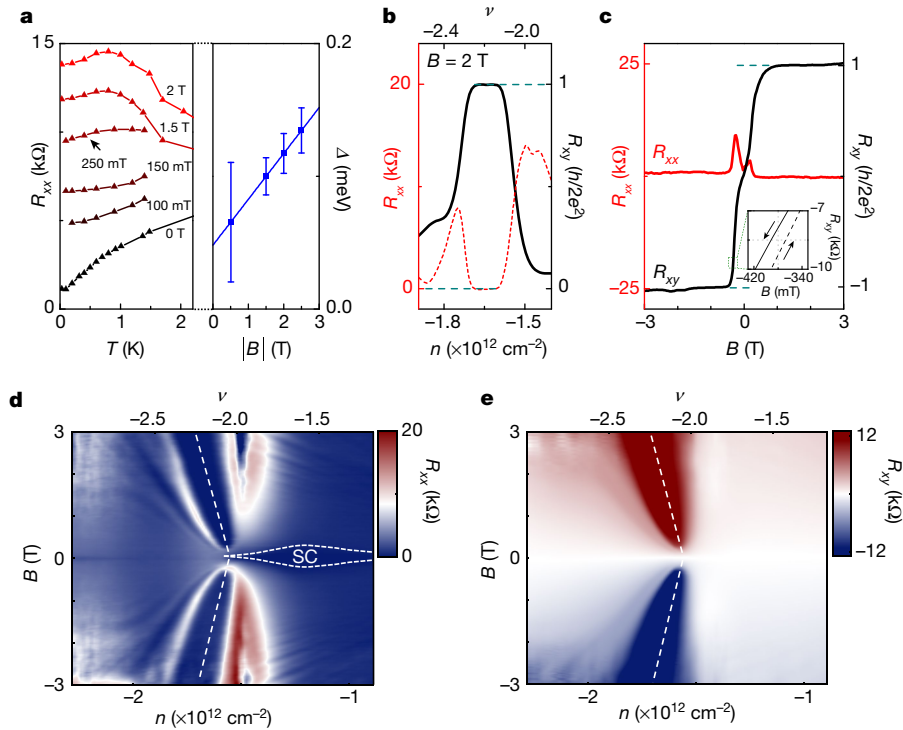
Fig. 3 | Formation of Chern insulators in small out of plane magnetic field. a, Left panel shows longitudinal sheet resistance R_{xx} versus temperature T for moiré band filling $\nu = -2$ for B fields from 0 T to 2 T. It reveals a transition from a metallic to a thermally activated behaviour $R_{xx} \approx \exp(\Delta/2k_B T)$, where the energy gap Δ increases linearly with B (right panel). The error bars show the full range of the fitting uncertainty. **b, c**, R_{xx} and transverse resistance R_{xy} versus charge carrier density n at $B = 2$ T (**b**) and versus B at $n = -1.75 \times 10^{12}$ cm^{-2} (**c**) shows quantization of $R_{xy} = h/2e^2$ and $R_{xx} = 0\ \Omega$ above $|B| \geq 0.4$ T. **d** and **e**, Colour plots of R_{xx} (**d**) and R_{xy} (**e**) versus n and B demonstrate the developing wedge-shaped phase diagram of a Chern insulator. h, Planck's constant.

correlated insulating fillings and strong thermally activated transport (Fig. 2a, b), which are accompanied by a novel set of quantum oscillations and Hall density offsets in the magnetic field. Here the superconductivity domes directly flank the correlated insulators with T_c values that range from 150 mK to 3 K; however, at integer fillings correlated insulators always persist. Device D2, with an intermediate w value and a θ slightly smaller than θ_m, displays features present in both D1 and D3. Although it does not display correlated insulators in the valence band, it shows a single superconductivity dome with a $T_c \approx 400$ mK. In the conduction band it features a non-activated resistance peak at $\nu = 2$, suggesting an underdeveloped correlated insulator, and two superconductivity domes flanking it, with $T_c \approx 500$ mK and $T_c \approx 650$ mK.

Overall, these findings clearly show that superconductivity in MATBG can exist independently of correlated insulating states, indicating that these phases are in competition with one another rather than share a common microscopic origin. Whereas insulating states are quenched in D1 and D2, the corresponding superconducting T_c values remain almost unaffected, falling in the same $T_c \approx 500$ mK–1.5 K range that was previously reported for the devices with similar twist angles, but in the presence of strong insulators[2–5]. Because both the screening and bandwidth effects affect U/t, it is difficult to completely disentangle these effects from the datasets at present available. Comparison with the limited data from the literature[1–5], however, indicates that screening may be a dominant effect in D1 ($\theta \approx 1.15°$) and D2 (1.04°), because these are the only reported devices[1,3–5] that do not show any signatures of correlated insulating states so close to the magic angle of 1.1°.

We further examine the transport properties of device D1 in a perpendicular magnetic field B. For $B > 0.3$ T an insulating gap Δ develops at exactly $\nu = -2$ filling, which is evident from a transition from a metallic to an activated transport behaviour (Fig. 3a). Fitting the longitudinal resistance with $R_{xx} \approx \exp(\Delta/2k_B T)$ for different B-field values shows an approximately linear evolution of Δ as a function of B (here k_B is the Boltzmann constant). The observed magnetoresistance can be attributed to field-induced quenching of the electron dynamics, where the magnetic field 'freezes' the kinetic energy t of the electrons by creating an Aharonov–Bohm flux through each moiré supercell[23–27]. This can tip the balance between the kinetic energy and Coulomb interaction in favour of the latter, producing an increase of the U/t ratio and the recurrence of the correlated insulating order.

Strikingly, at the same low-B fields at which the correlated insulator appears, a quantized Hall state develops. At fields as low as $B \approx 0.4$ T we observe regions of near-perfectly quantized plateaus of Hall resistance $R_{xy} \approx h/2e^2 = 12.9$ kΩ (with e the electron charge and h Planck's constant), accompanied by a vanishing $R_{xx} \approx 0\ \Omega$ (Fig. 3b, c). These values are consistent with the degeneracy of the expected correlated insulators at half filling[1] and are two times smaller than the free-electron values. Starting from $\nu = -2$ at $B = 0$, this state forms in a broad wedge-like region in the n–B phase space, extending to larger densities as B increases; the wedge boundary follows a dn/d$B = 2e/h$ dependence that is consistent with a Chern number of 2 (Fig. 3d, e).

The B field at which this quantized Hall state appears is almost an order of magnitude lower than the one needed to quantize all other quantum Hall plateaus in the system, $B > 3$ T (Extended Data Fig. 7). This state appears in the absence of single-particle Landau level quantization in the system, which suggests a different mechanism, probably originating from electron–electron interactions. This scenario is supported by the appearance of the symmetry broken correlated insulating state at $\nu = -2$ at the same B field. Theory predicts that strong correlations can favour a valley-polarized Chern insulator even for untwisted bilayer graphene[28,29]; however, in topological flat bands in MATBG, correlations are expected to boost and further strengthen the Chern insulator order[30]. Similar observations were recently made in hBN-aligned[6,7] and

Article

non-aligned MATBG[5] and in ABC trilayer graphene[16] for odd-integer filled states, where orbital magnetic states were proposed. A sizeable hysteresis around $B \approx 0.4$ T in device D1 potentially signals the existence of a similar state[19].

What are the implications of these findings for the origin of the superconducting state? The observed resilience of superconductivity upon suppression of the insulating phase is consistent with the two phases competing rather than being intimately connected. Such competition would be hard to reconcile with a common microscopic mechanism of the two phases as suggested by an analogy with cuprates. Instead, it appears that Coulomb interactions drive the formation of the commensurate insulators, whereas superconductivity arises from a more conventional mechanism. However, the anomalous character of superconductivity in MATBG, occurring at record-low carrier densities, suggests that the electron–phonon mechanism, if present, is enhanced by the high density of states and electron correlation effects. The reappearance of the correlated insulator phases in abnormally weak magnetic fields confirms that correlations remain strong in the system, calling for a better understanding of their impact on the superconducting order.

Online content

Any methods, additional references, Nature Research reporting summaries, source data, extended data, supplementary information, acknowledgements, peer review information; details of author contributions and competing interests; and statements of data and code availability are available at https://doi.org/10.1038/s41586-020-2459-6.

1. Cao, Y. et al. Correlated insulator behaviour at half-filling in magic-angle graphene superlattices. *Nature* **556**, 80–84 (2018).
2. Cao, Y. et al. Unconventional superconductivity in magic-angle graphene superlattices. *Nature* **556**, 43–50 (2018).
3. Kim, K. et al. Tunable moiré bands and strong correlations in small-twist-angle bilayer graphene. *Proc. Natl Acad. Sci. USA* **114**, 3364–3369 (2017).
4. Yankowitz, M. et al. Tuning superconductivity in twisted bilayer graphene. *Science* **363**, 1059–1064 (2019).
5. Lu, X. et al. Superconductors, orbital magnets and correlated states in magic angle bilayer graphene. *Nature* **574**, 653–657 (2019).
6. Sharpe, A. L. et al. Emergent ferromagnetism near three-quarters filling in twisted bilayer graphene. *Science* **365**, 605–608 (2019).
7. Serlin, M. et al. Intrinsic quantized anomalous Hall effect in a moiré heterostructure. *Science* **367**, 900–903 (2019).
8. Xie, Y. et al. Spectroscopic signatures of many-body correlations in magic-angle twisted bilayer graphene. *Nature* **572**, 101–105 (2019).
9. Kerelsky, A. et al. Maximized electron interactions at the magic angle in twisted bilayer graphene. *Nature* **572**, 95–100 (2019).
10. Jiang, Y. et al. Charge order and broken rotational symmetry in magic-angle twisted bilayer graphene. *Nature* **573**, 91–95 (2019).
11. Choi, Y. et al. Electronic correlations in twisted bilayer graphene near the magic angle. *Nat. Phys.* **15**, 1174–1180 (2019).
12. Goodwin, Z. A. H., Corsetti, F., Mostofi, A. A. & Lischner, J. Twist-angle dependence of electron correlations in moiré graphene bilayers. *Phys. Rev. B* **100**, 121106 (2019).
13. Pizarro, J. M., Rösner, M., Thomale, R., Valentí, R. & Wehling, T. O. Internal screening and dielectric engineering in magic-angle twisted bilayer graphene. *Phys. Rev. B* **100**, 161102 (2019).
14. Lee, P. A., Nagaosa, N. & Wen, X.-G. Doping a Mott insulator: physics of high-temperature superconductivity. *Rev. Mod. Phys.* **78**, 17–85 (2006).
15. Nilsson, F., Karlsson, K. & Aryasetiawan, F. Dynamically screened Coulomb interaction in the parent compounds of hole-doped cuprates: trends and exceptions. *Phys. Rev. B* **99**, 075135 (2019).
16. Chen, G. et al. Tunable correlated Chern insulator and ferromagnetism in trilayer graphene/boron nitride moiré superlattice. *Nature* **579**, 56–61 (2020).
17. Liu, X. et al. Spin-polarized correlated insulator and superconductor in twisted double bilayer graphene. Preprint at https://arxiv.org/abs/1903.08130 (2019).
18. Ochi, M., Koshino, M. & Kuroki, K. Possible correlated insulating states in magic-angle twisted bilayer graphene under strongly competing interactions. *Phys. Rev. B* **98**, 081102 (2018).
19. Xie, M. & MacDonald, A. H. On the nature of the correlated insulator states in twisted bilayer graphene. *Phys. Rev. Lett.* **124**, 097601 (2020).
20. Dodaro, J. F., Kivelson, S. A., Schattner, Y., Sun, X. Q. & Wang, C. Phases of a phenomenological model of twisted bilayer graphene. *Phys. Rev. B* **98**, 075154 (2018).
21. Po, H. C., Zou, L., Senthil, T. & Vishwanath, A. Faithful tight-binding models and fragile topology of magic-angle bilayer graphene. *Phys. Rev. B* **99**, 195455 (2019).
22. Zou, L., Po, H. C., Vishwanath, A. & Senthil, T. Band structure of twisted bilayer graphene: emergent symmetries, commensurate approximants, and Wannier obstructions. *Phys. Rev. B* **98**, 085435 (2018).
23. Dean, C. R. et al. Hofstadter's butterfly and the fractal quantum Hall effect in moiré superlattices. *Nature* **497**, 598–602 (2013).
24. Hunt, B. et al. Massive Dirac fermions and Hofstadter butterfly in a van der Waals heterostructure. *Science* **340**, 1427–1430 (2013).
25. Ponomarenko, L. A. et al. Cloning of Dirac fermions in graphene superlattices. *Nature* **497**, 594–597 (2013).
26. Nandkishore, R. & Levitov, L. Dynamical screening and excitonic instability in bilayer graphene. *Phys. Rev. Lett.* **104**, 156803 (2010).
27. Nandkishore, R. & Levitov, L. Quantum anomalous Hall state in bilayer graphene. *Phys. Rev. B* **82**, 115124 (2010).
28. Weitz, R. T., Allen, M. T., Feldman, B. E., Martin, J. & Yacoby, A. Broken-symmetry states in doubly gated suspended bilayer graphene. *Science* **330**, 812–816 (2010).
29. Young, A. F. et al. Tunable symmetry breaking and helical edge transport in a graphene quantum spin Hall state. *Nature* **505**, 528–532 (2014).
30. Bultinck, N. et al. Ground state and hidden symmetry of magic angle graphene at even integer filling. Preprint at https://arxiv.org/abs/1911.02045 (2019).

Methods

Screening layer fabrication process

The samples are fabricated using the "cut-and-stack" method, in analogy to the previously introduced "tear-and-stack" technique[3]. Typically, a thin hBN flake is picked up by a propylene carbonate (PC) film, which is placed on a polydimethyl siloxane (PDMS) stamp at 90 °C (Extended Data Fig. 1). The hBN flake is then used to pick up a part of a pre-cut monolayer graphene flake, mechanically exfoliated on a Si^{++}/SiO_2 (285 nm) surface. Subsequently, the second half of a graphene sheet is rotated to a target angle usually around $\theta \approx 1.1°$–$1.15°$ and then picked up by the hBN/graphene stack on the PC from the previous step. The heterostructure is then placed on top of another thin hBN flake. Usually, the bottom hBN flake thickness is chosen by optical contrast and further confirmed with atomic force microscopy (AFM) measurements. The very bottom layer of the heterostructure consists of a relatively thick graphite flake (typically a few layers of graphene >1 nm thick) that acts as a local back gate and a screening layer simultaneously. The final stack is then placed on a target Si^{++}/SiO_2 (285 nm) wafer, where it is further etched into a multiple Hall bar geometry using CHF_3/O_2 plasma and edge-coupled to Cr/Au (5 nm/50 nm) metal contacts.

Dielectric thickness measurements

The bottom hBN thickness is obtained from AFM measurements. Extended Data Fig. 2 demonstrates a set of MATBG heterostructures that have been used to fabricate the devices reported in the main text. The upper panel shows an optical image of the final graphite/hBN/MATBG/hBN stack. We find that the heterostructures exhibit high structural homogeneity and do not show visible bubble formations, which are known to locally distort the twist angle and charge carrier density. These observations are further confirmed by the AFM scans shown in the insets. The AFM scans are also used to extract the topography of the fabricated stacks, where we find hBN thicknesses of $w \approx 7.0$ nm (D1), 9.8 nm (D2) and 12.5 nm (D3).

The difference in bottom dielectric thickness is further confirmed by measurements of the capacitance between the graphite and the MATBG layers. Using the quantum oscillations map (Extended Data Fig. 7), we find that the back gate capacitance changes from 355 nF cm^{-2} (D1) to 260 nF cm^{-2} (D2) and further to 221 nF cm^{-2} (D3), in a good agreement with the extracted AFM height profiles.

Effects of disorder in our devices

During the stacking procedure, twist angle disorder may be introduced into the final heterostructure. To further analyse the twist angle homogeneity, we perform two-terminal conductance measurements versus carrier density for different sets of contact pairs, as shown in Extended Data Fig. 3 for device D1. Contact pairs on the right-hand side of the sample (A–B, B–C, C–D, and D–E) demonstrate the highest angle homogeneity with maximum charge carrier density deviation of the full filled superlattice unit cell $\delta n_s^{max} \approx 0.03 \times 10^{12}$ cm^{-2}. Of the contact pairs, C–D was used to obtain longitudinal resistance data R_{xx} in this device. Overall, because the positions of the band-insulator gaps match exceptionally well, the graph demonstrates high global twist angle homogeneity. The position of the CNP varies little between the different contact pairs ($V_g^{CNP} = -4 \pm 1$ mV).

In addition, we perform the analysis on the full-width at half-maximum (FWHM) of the resistance peak at the CNP, and the sharpness of the bandgap edges at complete filling of the moiré bands. We estimate a charge carrier inhomogeneity at CNP of $\delta n \approx 1.8 \times 10^{10}$ cm^{-2}, which suggests that the sample inhomogeneity is mainly defined by charge disorder. Moreover, all devices show very small twist-angle inhomogeneity, with variation as small as $\Delta\theta \approx 0.01°$ per 10 µm (Supplementary Information), with robust, macroscopic superconducting regions spanning the entire device area, which we confirmed by transport measurements

using different contact pairs across the device (Fig. 1f). Here we note that in a situation where disorder would mix the superconductivity and correlated insulating phases in the sample, a percolating superconductivity network could in principle short-circuit the correlated insulating phases. However, the exceptionally low level of the charge inhomogeneity and twist-angle disorder makes such a scenario highly unlikely.

Superlattice density extraction

The phase diagram shown in Extended Data Fig. 7 is used to estimate the twist angles in the measured devices. We use the relation $n_s \approx 8\theta^2/\sqrt{3}a^2$, where $a = 0.246$ nm is the lattice constant of graphene and n_s is the charge carrier density corresponding to a fully filled superlattice unit cell. Quantum oscillations propagating outside of the fully filled flat band (for example, see the black solid and dashed lines in Extended Data Fig. 7) converge at a point on the horizontal axis that defines n_s. Using this position, we find that $n_s \approx 3.04 \times 10^{12}$ cm^{-2} (or in terms of absolute gate voltage values, $V_g - V_g^{CNP} \approx 1.38$ V). This constitutes a twist angle in D1 of $\theta \approx 1.15°$.

Transport measurements

All measurements were carried out in a dilution refrigerator under an out-of-plane magnetic field B. For transport measurements we have employed a standard low-frequency lock-in technique using Stanford Research SR860 amplifiers with excitation frequency $f = 19.111$ Hz. To control the back gate voltage, we use Keithley 2400 s voltage source meters. Direct-current (d.c.) voltage versus d.c. excitation current measurements are performed using SR560 low-noise d.c. voltage preamplifier in combination with a Keithley 2700 multimeter. To achieve a lower electron temperature in our measurements, we (1) perform electronic filtering of the measurement setup using a network of commercially available low-pass RC and LC filters and (2) use very low excitation currents (<10 nA) owing to the risk of overheating electrons and the fragility of superconductivity phases. Alternating-current excitation currents are applied through a 10-MΩ resistor. All data in this study is taken at the fridge base temperature of about 20–30 mK unless specified.

Data availability

The data that support the findings of this study are available from the corresponding author upon reasonable request.

Author contributions D.K.E, X.L. and P.S. conceived and designed the experiments. P.S., X.L. and I.D. performed the experiments. P.S. and D.K.E. analysed the data. A.F. and L.L. performed the theoretical modelling. T.T. and K.W. contributed materials. D.K.E. and F.H.L.K. supported the experiments. D.K.E, L.L. and P.S. wrote the paper.

a

PC

hBN ↓

Graphene

Si⁺⁺/SiO₂

b

Twist by
θ ≈1.10-1.15°

PC

hBN ↓

Si⁺⁺/SiO₂

c

PC

hBN ↓

MAG →

Dielectric
spacer

hBN

Si⁺⁺/SiO₂

d

PC

hBN ↓

hBN

FLG
(screening layer)

Si⁺⁺/SiO₂

**e**

Final stack

hBN

hBN

Dielectric
spacer

Si⁺⁺/SiO₂
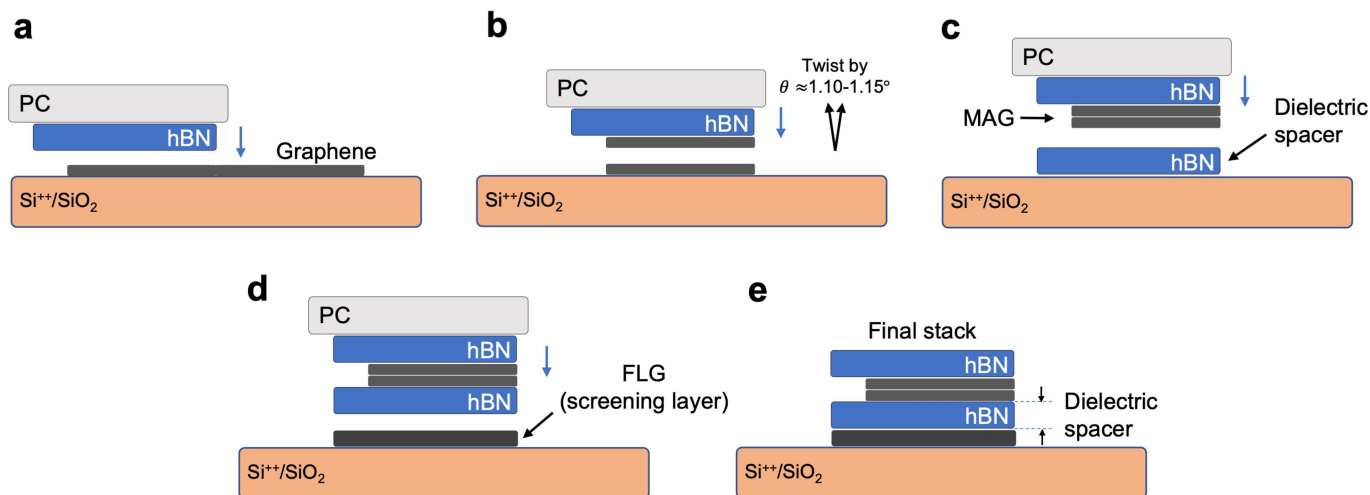
Extended Data Fig. 1 | Screening layer fabrication method. a, The sacrificial PC layer is used to pick up the top hBN, which is further used to pick up the first half of a monolayer graphene flake. **b**, The second half of the graphene flake is rotated by 1.10° to 1.15° and subsequently picked up by the hBN/graphene stack on the PC. **c**, The heterostructure is further placed on the bottom hBN, which serves as a dielectric spacer. **d, e**, At the final step the heterostructure is placed on top of the target wafer and the PC layer is removed with chloroform.
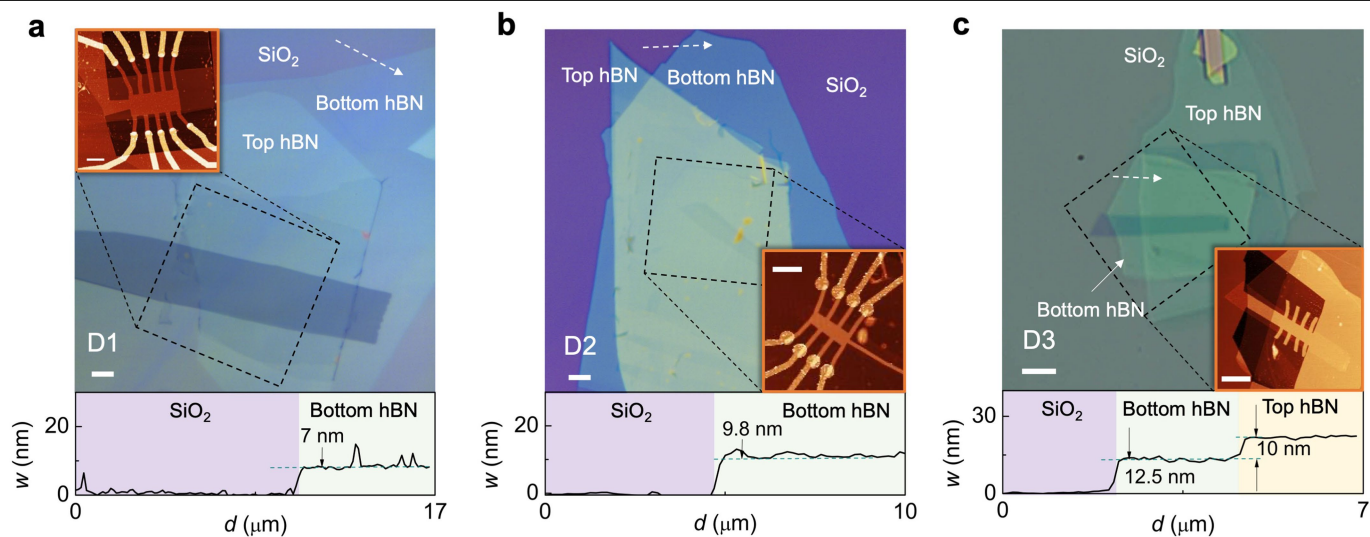
Extended Data Fig. 2 | AFM and optical micrographs for samples D1, D2 and D3. a, D1; **b**, D2; **c**, D3. The main panels are optical images of the final stacks, from which all three devices were fabricated. The insets demonstrate AFM scans of the final devices etched into multi-terminal Hall bar geometries. The dashed black squares show AFM image areas. The bottom hBN thickness measurements are shown on the lower panels. Height profiles are taken along the white dashed arrow lines. Scale bars, 5 μm.
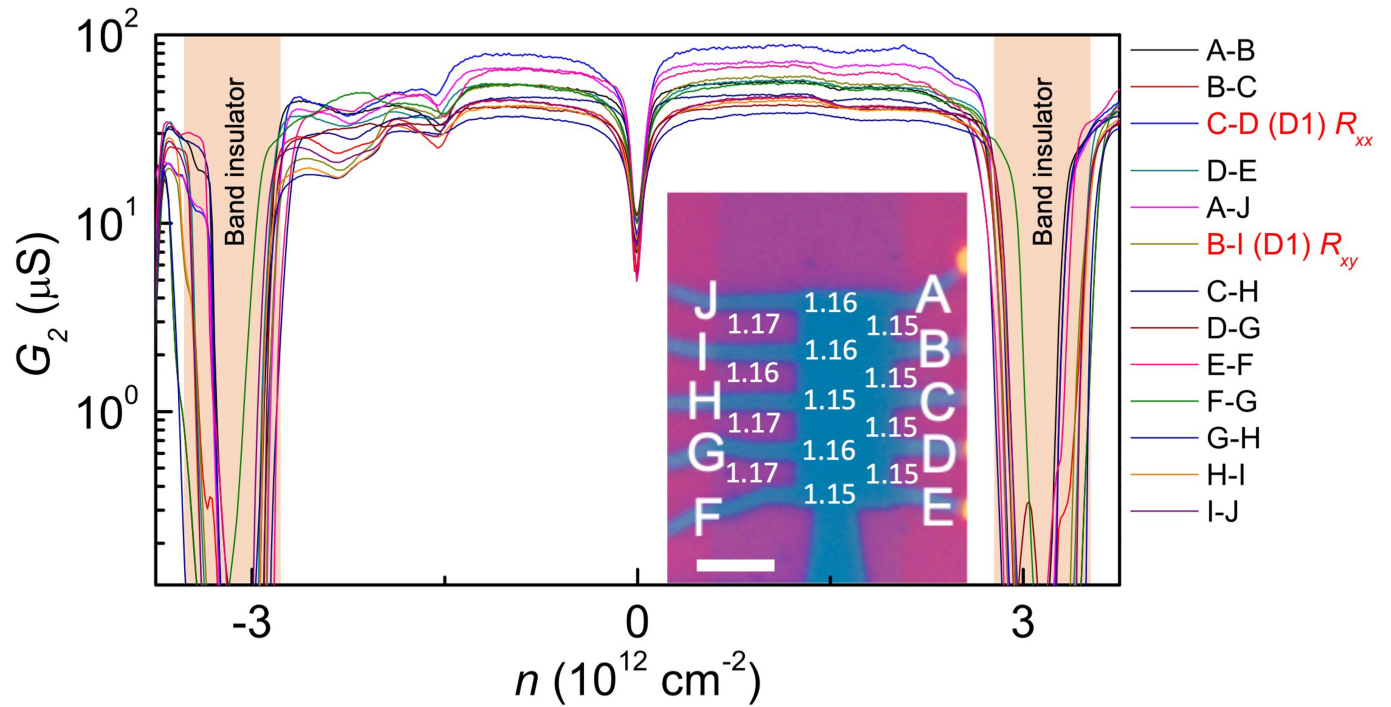
Extended Data Fig. 3 | Two-terminal conductance measurements across all available contacts in device D1. The key shows two-terminal conductance measurements G_2 between different contact pairs corresponding to the inset optical image of the device. Numbers on the device optical micrograph correspond to measured global twist angle values between contact pairs (extracted from resistance maxima). Scale bar, 5 μm. Data are taken at 20 mK.
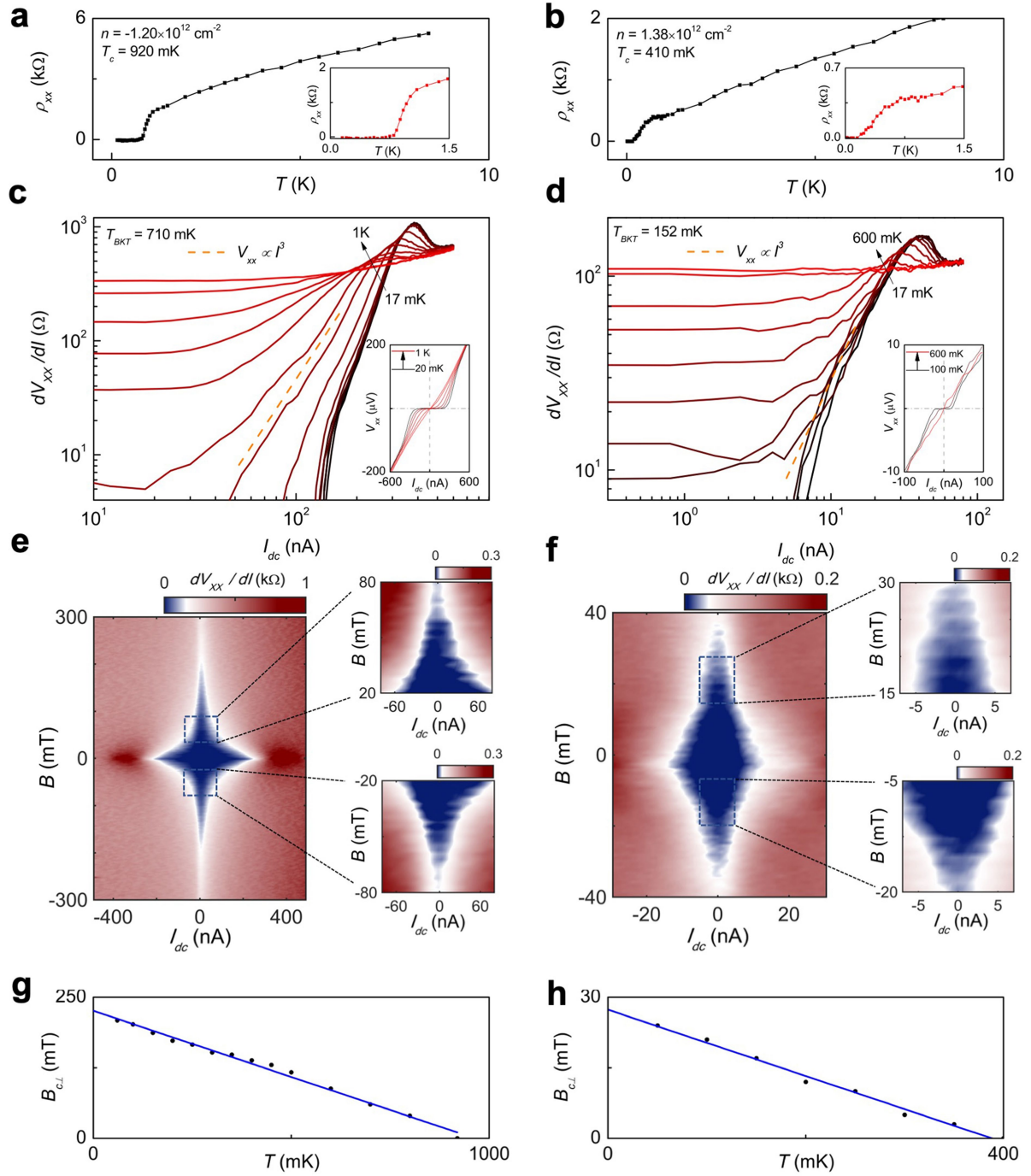
Extended Data Fig. 4 | Superconductivity state characterization in device D1. The right- (left-) hand panels refers to the superconductivity pocket in the valence (conductance) band on the top panel of Fig. 1c. **a**, **b**, Temperature activation of superconductivity for both pockets on the absolute resistivity scale. The insets demonstrate a zoomed-in range of temperatures from 0 K to 1.5 K. **c**, **d**, Berezinskii–Kosterlitz–Thouless (BKT) measurements of differential resistance dV_{xx}/dI versus d.c. current bias I_{dc} for both superconductivity pockets. The insets show d.c. voltage as a function of d.c. current bias taken at different temperatures for optimally doped superconductivity states.

e, **f**, Differential conductance dV_{xx}/dI (colour scales) as a function of perpendicular magnetic field B and d.c. current bias I_{dc} shows distinct diamond-like features for both pockets. Zoomed-in images (to the right of each panel) show clear Fraunhofer interference patterns, which are a firm proof of superconductivity. **g**, **h**, Ginzburg–Landau coherence length measurements for both pockets. Critical field $B_{c\perp}$ versus critical temperature T_c taken at half the normal state resistance values. Black dots refer to experimentally obtained values; blue lines are linear fits to the data. We estimate coherence lengths $\xi_{GL} = 38$ nm (**g**) and $\xi_{GL} = 101$ nm (**h**).
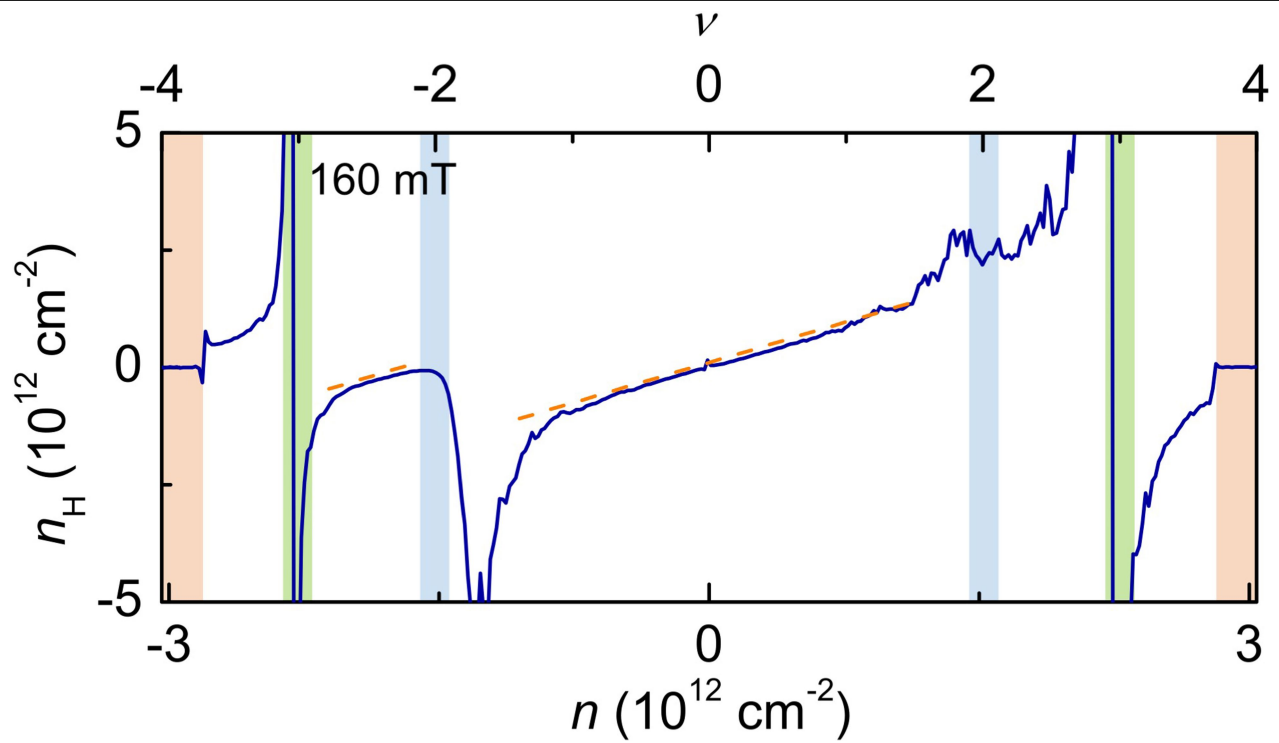
Extended Data Fig. 5 | Hall density measurements in device D1. Hall density n_H versus charge carrier density n extracted from the low-field Hall resistance measurements at 160 mT.
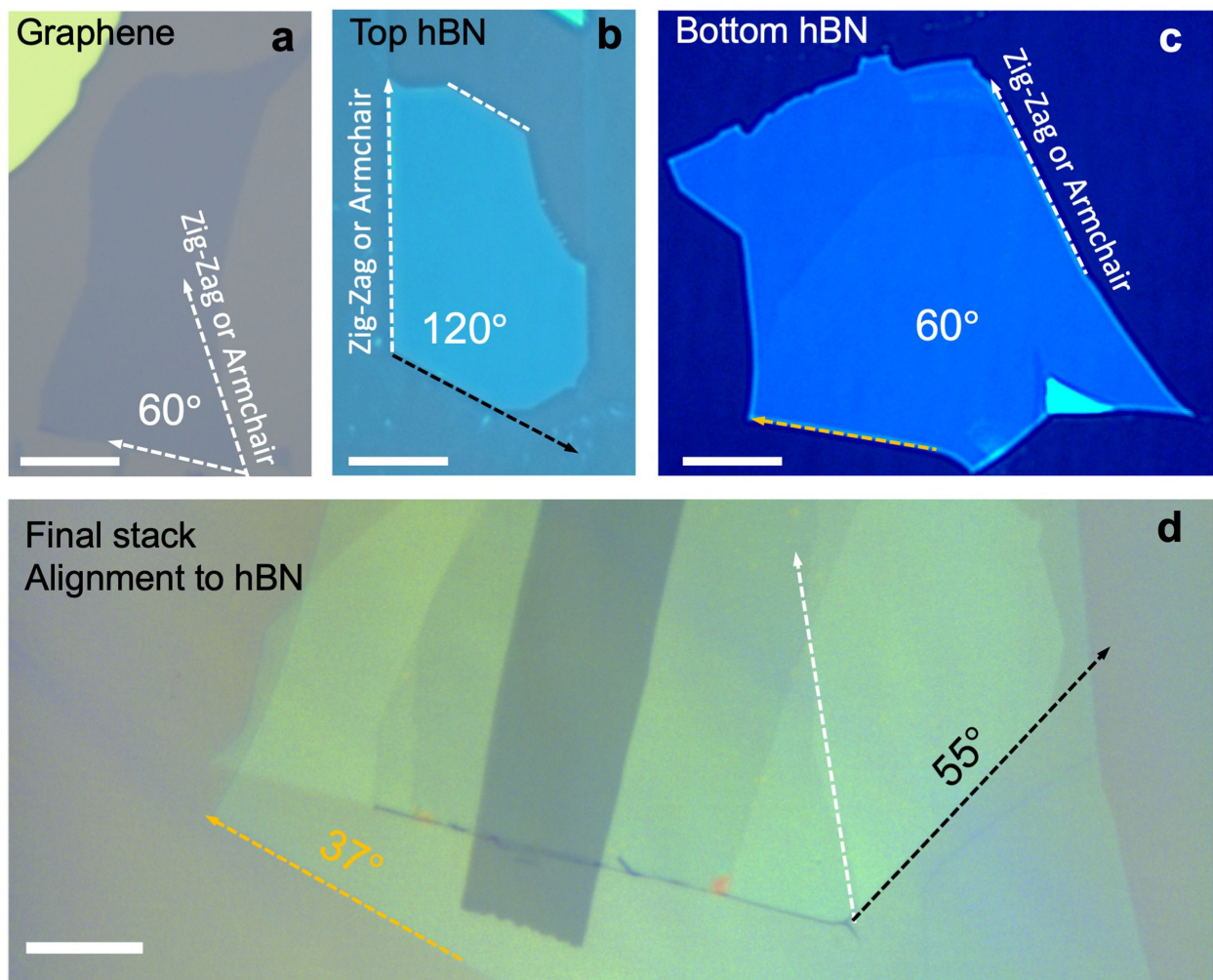
Extended Data Fig. 6 | Check for alignment to hBN. a, Optical image of the monolayer graphene flake on SiO₂ substrate used for fabrication of the MATBG heterostructure. White dashed arrows indicate preferable lattice directions (zig-zag or armchair). **b**, Optical image of the top hBN flake. **c**, Optical micrograph of the bottom hBN flake. **d**, Optical image of the final stack on SiO₂ substrate. The black dashed arrow indicates the edge of the top hBN shown in **b**. The orange dashed arrow corresponds to the edge of the bottom hBN shown in panel **c**. Black (orange) numbers correspond to the angle between the white dashed arrow (graphene edge) and the top (bottom) hBN. We estimate the twist angle between the bottom hBN and MATBG to be about 7(±1.5)° or 23(±1.5)° and between the top hBN and MATBG to be about 25(±1.5)° or 5(±1.5)°. Furthermore, we do not find signatures of alignment to hBN in the magnetic field Shubnikov–de Haas oscillation data for any of the three devices (for example, Extended Data Fig. 7). Scale bars, 20 μm.
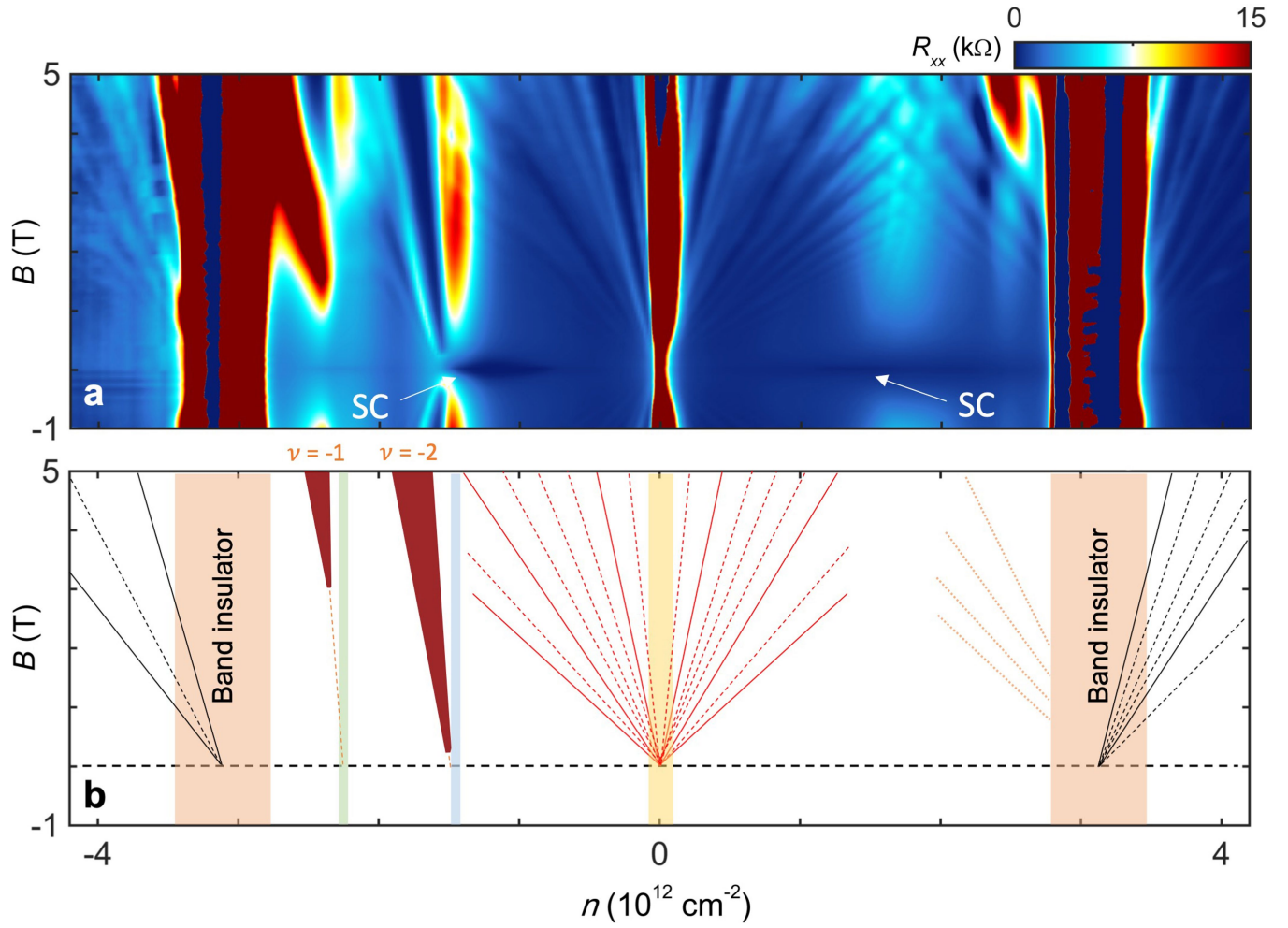
Extended Data Fig. 7 | Full range magnetic field phase diagram in device D1 at 30 mK. a, Longitudinal sheet resistance R_{xx} (colour scale) versus change carrier density n and perpendicular magnetic field B. **b**, Schematic image of Landau levels shown in **a**. Solid lines correspond to fourfold degenerate levels with quantized plateaus $\nu_{LL} = 4, 8, 12, …$ Dashed lines show broken spin and/or valley degeneracy levels. Dark red features to the left show Chern-like insulator states originating from ($\nu = -2$)-filled or ($\nu = -3$)-filled superlattice unit cell corresponding to quantization of $2e^2/h$ (or of e^2/h). Blue and green shaded stripes on the left correspond to the superlattice unit cell with commensurate fillings $\nu = -2$ and -3, respectively.
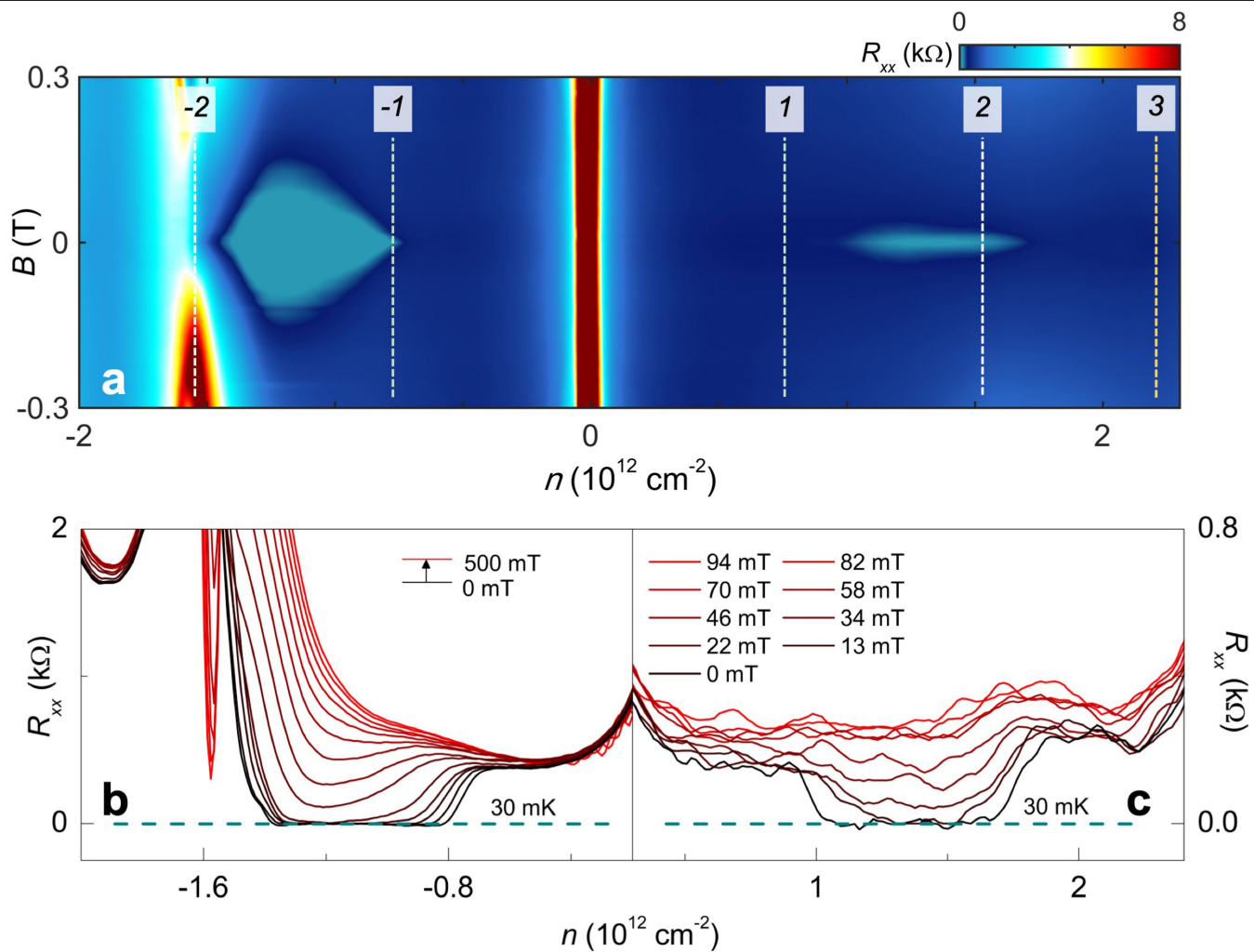
Extended Data Fig. 8 | Effect of low magnetic field on correlated states in device D1. a, Longitudinal sheet resistance R_{xx} (colour scale) versus charge carrier density n and perpendicular magnetic field B. $I_{ac} = 10$ nA. **b**, R_{xx} as a function of charge carrier density n for valence band superconductivity pockets in **a**. $I_{ac} = 10$ nA. **c**, Resistance versus charge carrier density for valence band superconductivity pockets in **a**. $I_{ac} = 1$ nA.